nature nanotechnology

Article

https://doi.org/10.1038/s41565-024-01791-2

Controlled single-electron transfer enables time-resolved excited-state spectroscopy of individual molecules

Received: 28 March 2024

Accepted: 19 August 2024

Published online: 26 September 2024

Check for updates

Lisanne Sellies[1] ✉, Jakob Eckrich[1], Leo Gross[2], Andrea Donarini[3] & Jascha Repp[1] ✉

An increasing number of scanning-probe-based spectroscopic techniques provides access to diverse electronic properties of single molecules. Typically, these experiments can only study a subset of all electronic transitions, which obscures the unambiguous assignment of measured quantities to specific quantum transitions. Here we develop a single-molecule spectroscopy that enables the access to many quantum transitions of different types, including radiative, non-radiative and redox, that is, charge-related, transitions. Our method relies on controlled alternating single-charge attachment and detachment. For read-out, the spin states are mapped to charge states, which we can detect by atomic force microscopy. We can determine the relative energies of ground and excited states of an individual molecule and can prepare the molecule in defined excited states. After a proof-of-principle demonstration of the technique on pentacene, we apply it to PTCDA, the scanning-probe luminescence of which has been interpreted controversially. The method may be used to guide, understand and engineer tip-induced chemical reactions as well as phosphorescence and fluorescence of individual molecules.

The combination of scanning-probe microscopy with an increasing number of spectroscopic techniques provides insight into the properties of individual molecules at their intrinsic atomic scale. Examples of such single-molecule studies with atomic-scale local information encompass structure determination[1], orbital density imaging[2] and electron-spin resonance[3,4]. In particular, the integration of optical spectroscopy into local-probe microscopy such as Raman[5] and luminescence[6] has recently provided atomic-scale insights into light–matter interaction: theoretical concepts can now be tested and visualized directly in space providing an understanding of the fundamental processes in light emission from organic materials[7].

Despite its very direct access to well-defined single-molecule model systems, the unambiguous assignment of observations to specific electronic quantum transitions is not always straightforward. For example, the assignment of a scanning tunnelling microscopy (STM) luminescence signal as phosphorescence or trion-related fluorescence is contradictory in recent literature[8,9]. Similarly, in scanning tunnelling spectroscopy (STS), the discrimination of energetically higher-lying excited states from multiple charging effects is usually difficult[10,11]. One issue is that in STS the molecule typically reverts to its ground state, since a tip-to-molecule tunnelling event is followed by a quick molecule-to-substrate tunnelling event, and the two events are not detected separately. As the charge exchange with the surface is elusive in most STM experiments, it is in some cases very challenging to discern the different processes. For example, in STS, a feature at a higher bias voltage than required for tunnelling into the lowest unoccupied molecular orbital (LUMO) might be associated to either electron tunnelling into the LUMO+1 or to tunnelling of a second electron into the LUMO starting from a transient charge state. Even upon combining techniques such as luminescence with tunnelling

[1]Institute of Experimental and Applied Physics, University of Regensburg, Regensburg, Germany. [2]IBM Research Europe—Zurich, Rüschlikon, Switzerland. [3]Institute of Theoretical Physics, University of Regensburg, Regensburg, Germany. ✉e-mail: lisanne.sellies@ur.de; jascha.repp@ur.de

https://doi.org/10.1038/s41565-024-01791-2

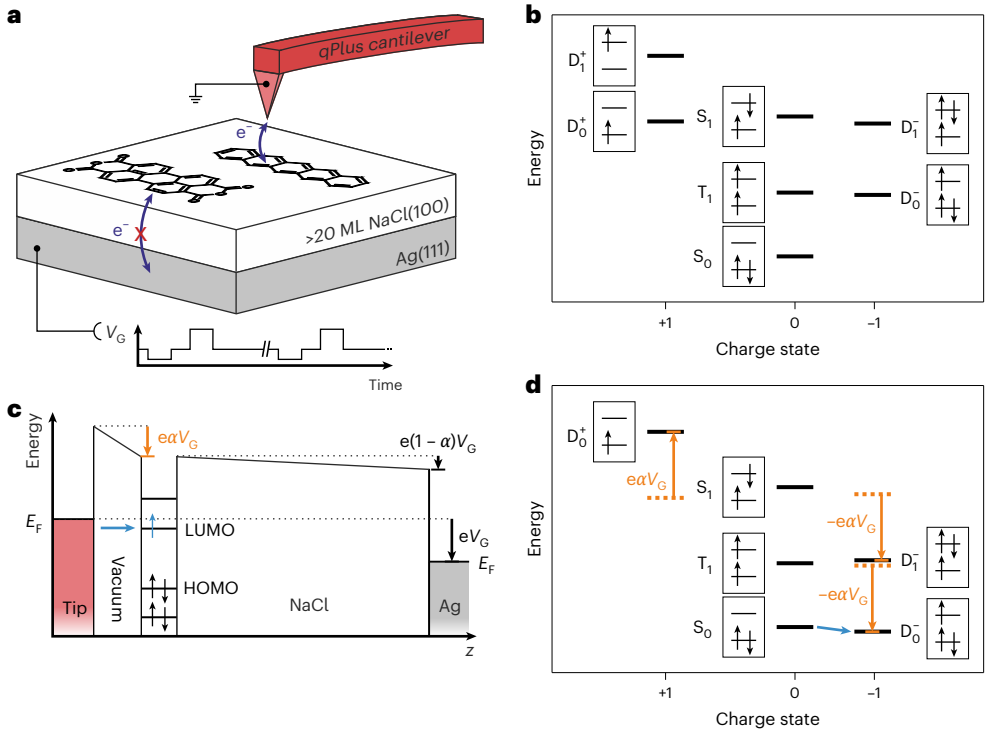

Fig. 1 | Experimental set-up, energy-level diagrams and gating. a, Sketch of the experimental set-up. Molecules (pentacene and PTCDA) were deposited on a >20 ML thick NaCl film that prevents tunnelling to the underlying Ag(111) substrate. A pump–probe voltage pulse sequence was applied to steer single-electron tunnelling between the tip and the molecule. **b**, Many-body energy diagram of the electronic states of a typical molecule with a closed-shell ground state. S, D and T refer to singlet, doublet and triplet states, respectively. The small diagrams depict the electronic configuration, that is, the occupation of the HOMO (bottom) and LUMO (top). The relative energetic alignment of the states depends on the specific molecule, work function of the surface and the applied gate voltage V_G. **c**, Schematic of the double-barrier tunnelling junction. V_G shifts the molecular levels with respect to the Fermi level E_F of tip and Ag substrate. A part of V_G, that is, $(1-\alpha)V_G$, drops in the NaCl film, and the remainder, that is, αV_G, drops in the vacuum between the tip and the molecule. In the situation shown, the applied voltage enables tunnelling of an electron from the tip to the LUMO. To simplify the illustration, it implies that at $V_G = 0$, there is no electric field in the junction—without loss of generality for other situations. **d**, Many-body energy diagram showing the same gating and tunnelling processes as in **c**: tunnelling an electron into the LUMO of the ground-state molecule brings the molecule from the S_0 to the D_0^- state. The shifts of the energy levels owing to V_G with respect to E_F of the tip are indicated in orange. In the many-body diagram on thick films, tip–sample tunnelling events correspond to transitions that go downward in the many-body diagram (blue arrow; the corresponding tunnelling event is also indicated in **c**).

spectroscopy, studying the individual electronic transitions separately remains out of reach, since several electronic transitions lead to one spectral feature.

The use of insulating films, thick enough to prevent tunnelling of charges to and from the underlying support, allows separating the individual electronic transitions by controlling and measuring the tunnelling of single electrons between a conductive tip of an atomic force microscope and a single molecule[4,12–16]. At the same time, several of the molecule's charge states become accessible[17]. While select transitions between electronic states were measured[18], mapping out the excitation spectrum of an individual adsorbed molecule remained out of reach.

In this Article, building on these developments, we propose a single-molecule spectroscopy method that allows probing many quantum transitions of different types individually, including radiative, non-radiative and redox transitions, in which the charge state changes. By controlled charge exchange between the conductive tip of an atomic force microscope and the molecule, we bring the latter into different electronic configurations, including those with different net charges. The detection proceeds via the force acting on the probe tip[13,14]. Guided by the different characteristic lifetimes of the states, we can thereby energetically map out the low-energy electronic states of individual molecules. We demonstrate the power of this spectroscopy by applying it to pentacene and perylenetetracarboxylic dianhydride (PTCDA), thereby shedding light on the interpretation of the recent prominent STM-induced luminescence experiments on PTCDA[8,9].

Excitation and read-out scheme

A schematic of the experimental set-up is shown in Fig. 1a. Pentacene and PTCDA molecules were deposited on a thick NaCl film (>20 monolayers (ML)) on Ag(111), where the NaCl electrically isolates the molecules from the underlying metal[17]. Voltage pulses were applied as a gate voltage to the Ag(111) substrate. The gate voltage V_G controls the alignment of the molecular electronic states with respect to the Fermi level of the tip, and steers single-electron tunnelling between the tip and the molecule, used for mapping out the electronic transitions.

To guide the understanding and the interpretation of the results, we use a many-body description of the states. First, we consider a generic system of a molecule with a closed-shell ground state, without degeneracies of the frontier orbitals. Figure 1b shows the corresponding low-lying electronic states. Such molecules have the singlet state S_0 as the ground state, in which all electrons are paired up, filling the orbitals up to the highest occupied molecular orbital (HOMO). Typically, the lowest-lying excited states are formed by exciting one of the electrons from the HOMO to the LUMO. Thereby, either the first excited triplet state T_1 or the first excited singlet state S_1 is formed, which are separated by the exchange interaction of the two unpaired electrons. For some molecules, a second excited triplet state T_2 (not shown here) may be located energetically between T_1 and S_1. Upon removing or adding one electron, the doublet ground states D_0^+ and D_0^- of the charged molecule are formed, respectively. The corresponding lowest-lying

https://doi.org/10.1038/s41565-024-01791-2

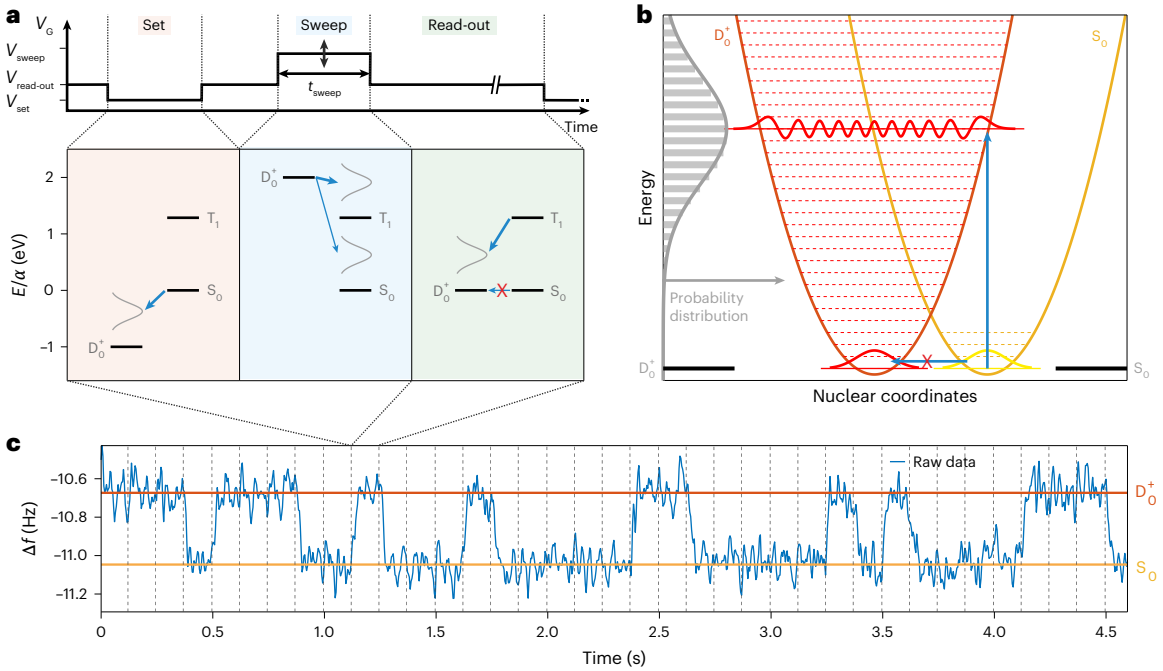

Fig. 2 | Pulse sequence, transition probabilities and read-out signal. a, Typical pump–probe voltage pulse sequence with the many-body energy diagrams (cf. Fig. 1b,d) showing possible transitions for the different phases of the sequence (only three states are shown for simplicity). Thicker arrows indicate dominating transitions (Supplementary Section 2). The molecule is initialized in a specific state (here D_0^+) by the set pulse with voltage V_{set}, followed by a sweep pulse with variable time t_{sweep} and voltage V_{sweep}. The states are subsequently mapped onto two different charge states using a read-out voltage $V_{read\text{-}out}$, which is adjusted such that two different charge states are degenerate. The different charge states can be discriminated by AFM. **b**, Franck–Condon picture of the strong coupling between net charges in the adsorbed molecule and phonons in the ionic film[23], depicted exemplarily for D_0^+ and S_0. Because of the strong coupling, the two states have their energy minimum at significantly shifted nuclear coordinates. Therefore, there is a vanishing overlap of their vibrational ground states (red and yellow Gaussians) such that zero-phonon transitions are blocked (crossed-out arrow). Consequently, for a gate voltage, for which the states are (close to) degenerate, the molecule becomes charge bistable. The Franck–Condon factors (horizontal grey bars) become large for high-lying vibrational states (the wavefunction, for which the overlap with the ground-state wavefunction is largest, is shown exemplarily). Considering a phonon bath, this results in a nearly Gaussian-shaped transition probability[23] (grey distribution), the maximum of which is offset to the ground state by the relaxation energy[22,23]. This Gaussian-shaped transition probability is indicated in the many-body diagrams (**a**), where transitions occur dissipatively from a vibrational ground state (black lines) to an excited vibrational state. **c**, Raw data trace measured for a pentacene molecule using the pump–probe voltage pulse sequence shown in **a**. The frequency shifts of the D_0^+ and S_0 states are indicated by the red and yellow lines, respectively. The dotted lines indicate the start of every pump–probe voltage pulse cycle. The duration of the set and sweep pulses is negligible against the duration of the read-out interval (125 ms).

excited states are D_1^+ and D_1^-, depicted here with one electron being excited from the HOMO to the LUMO. Throughout the paper, we refer to the orbital electronic levels according to the neutral molecule's states. Depending on the molecule under study, D_1^+ and D_1^- may instead involve an excitation from the HOMO-1 to HOMO or from LUMO to LUMO+1, respectively. In any case, D_1^+ and D_1^- are characterized by an exciton in the molecule that carries a net charge, also called trion. Note that many of the states are expected to have a multi-reference character. For instance, we find by modelling that the S_0 state described above has a non-zero contribution of a configuration with two electrons in the LUMO and none in the HOMO (Supplementary Section 12).

When comparing energies of states with different net charges in the many-body description on thick insulating films, one has to consider at which energy the molecule can exchange electrons with the tip. An applied V_G shifts the molecule's single-particle levels with respect to the Fermi level of the tip (Fig. 1c). This changes the energy of the many-body states with different net charges with respect to each other while leaving the energy differences within one charge state unaltered. Specifically, V_G will shift the states by $q\alpha V_G$, with q being the net charge of the molecule and α the lever arm[19–21], thus shifting the positive (+) and negative (−) charge states in opposite directions (Fig. 1d). α is a constant scaling factor between V_G and the energy scale, because some part of the gate voltage V_G drops across the NaCl film located between the molecule and the supporting gate (Fig. 1c).

To acquire a spectrum, we repeatedly apply a pulse sequence to the gate voltage, controlling cycles of driven tunnelling events and charge-state detection. In each sequence, we first bring the molecule with a set pulse to a defined state, for example, the D_0^+ state (Fig. 2a). Subsequently, a sweep pulse with a voltage V_{sweep} is applied, bringing the molecule via one or more tunnelling events to a variety of possible states. Finally, a read-out voltage is applied that corresponds to the charge-degeneracy point[17] between S_0 and one of the singly charged ground states, that is, D_0^+ or D_0^- (refs. 4,16) (Fig. 2a). At this voltage, the resulting charge state is read out by means of the electrostatic force acting on the tip[14], as shown in Fig. 2c. Interconversion between the two degenerate charge states by single-electron tunnelling to/from the tip is prevented by the vanishing Franck–Condon overlap[22] between their vibrational ground states owing to the large electron–phonon coupling. The Franck–Condon factors become large for much higher-lying vibrational states. Considering a phonon bath, this results in a Gaussian-shaped transition probability[23] (Fig. 2b). These Gaussian-shaped transition probabilities being offset with respect to the vibrational ground states by the relaxation energies are schematically depicted in the many-body diagrams by rotated Gaussians (Fig. 2a).

This read-out scheme also allows differentiating certain electronic states that correspond to the same charge state. For example, S_0 and T_1 can be distinguished by projecting them onto different charge states[4,16],

https://doi.org/10.1038/s41565-024-01791-2

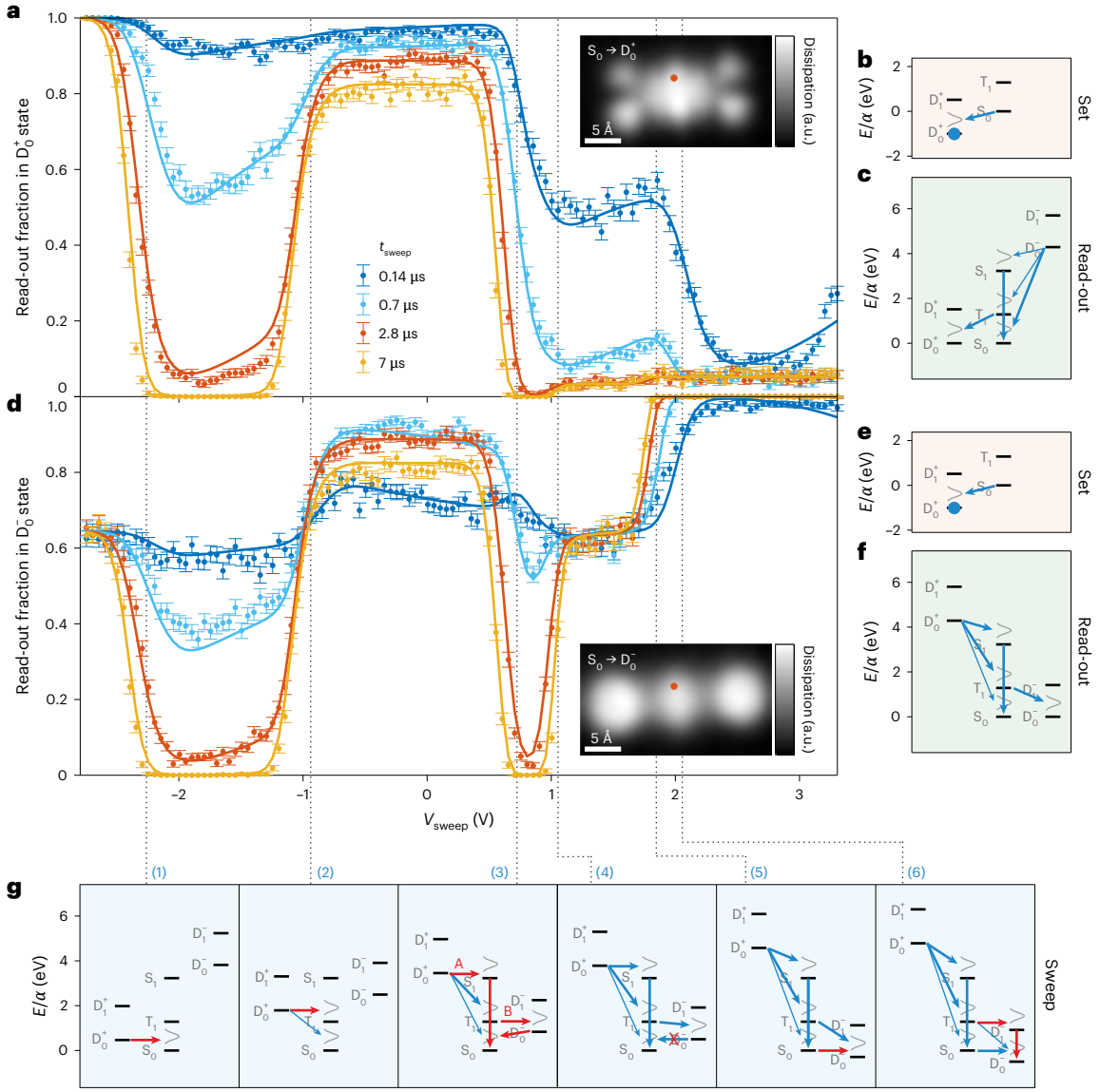

Fig. 3 | Excited-state spectroscopy of pentacene, initialized in the cationic charge state. a,**d**, Plot of the read-out fraction (normalized population during the read-out phase) in the D_0^+ (**a**) and D_0^- (**d**) states, respectively, as a function of V_{sweep}. The voltage pulse sequence was similar to Fig. 2a ($V_{set} = -3.795$ V), using $V_{read\text{-}out}$ at the S_0–D_0^+ ($V_{read\text{-}out} = -2.795$ V) and S_0–D_0^- ($V_{read\text{-}out} = 1.416$ V) degeneracies for **a** and **d**, respectively. Four different t_{sweep} were used, as indicated. Each data point corresponds to the normalized discrete counts of 640 pump–probe cycles and the error bars are ± s.d. of the binominal distribution (Methods). Solid lines represent fits to the data (Supplementary Sections 7 and 8). Vertical dotted lines are guides to the eye; for fitted threshold voltages, see Supplementary Table 1. AC-STM images[15] (insets) are measured for the same individual pentacene molecule (oscillation amplitude $A = 1$ Å): $S_0 \rightarrow D_0^+$ (HOMO), $\Delta z = -2.6$ Å, $V_G = -2.9$ V, $V_{a.c.} = 1.2$ V peak-to-peak (V_{pp}); $S_0 \rightarrow D_0^-$ (LUMO), $\Delta z = -2.0$ Å, $V_G = 1.43$ V, $V_{a.c.} = 1.2$ V_{pp}. The tip-height offset Δz is relative to the set point $\Delta f = -1.443$ Hz at $V = 0$ V, $A = 3$ Å. Red dots indicate the positions at which the spectra were measured. **b**,**c**,**e**,**f**, Many-body energy diagrams (cf. Fig. 1b,d) of the transitions taking place during the set pulse (**b**,**e**) and at the beginning of the read-out phase (**c**,**f**) for the spectra shown in **a** and **d**, respectively. The initialization state is indicated by a blue dot. **g**, Many-body energy diagrams at the sweep voltages indicated by the dotted lines. The process(es) that cause the change in the spectra around the indicated voltage are represented by red arrows (opening of transitions) and crosses (closing of transitions). At (3) two new transitions open, indicated with A and B, and referred to as (3A) and (3B). The opening of a certain transition (horizontal red arrows) may also enable a cascade of further transitions (downward red arrows in (3) and (6)). The relative thicknesses of the different arrows connecting two charge states roughly indicate the ratio of the rates governed by their tunnelling barriers (Supplementary Section 2).

such as S_0 and D_0^+, respectively. At the read-out voltage corresponding to the S_0–D_0^+ degeneracy point, the molecule will stay in S_0 if it was in S_0 at the end of the sweep pulse, while it will transit into D_0^+ if it was in T_1. In general, all the resulting states after each sweep pulse are mapped onto the two different charge states being degenerate at the read-out voltage. Upon repeating this voltage pulse sequence 8 times per second, typically for 80 s for a given V_{sweep}, the population in the two resulting charge states was determined as a function of V_{sweep} (Fig. 2c shows part of a measured atomic force microscopy (AFM) data trace for one V_{sweep}). The further V_{sweep} differs from V_{set}, the more transitions become possible, allowing us to infer the transitions during the sweep pulse and in turn the energetic alignment of the low-lying electronic states, as follows.

Excited-state spectroscopy on pentacene

Figure 3a shows the results of such an experiment for a single pentacene molecule, with read-out at the S_0–D_0^+ degeneracy. Here the set pulse prepares the molecule in D_0^+ (Fig. 3b). For V_{sweep} voltages close to $V_{read\text{-}out}$,

https://doi.org/10.1038/s41565-024-01791-2

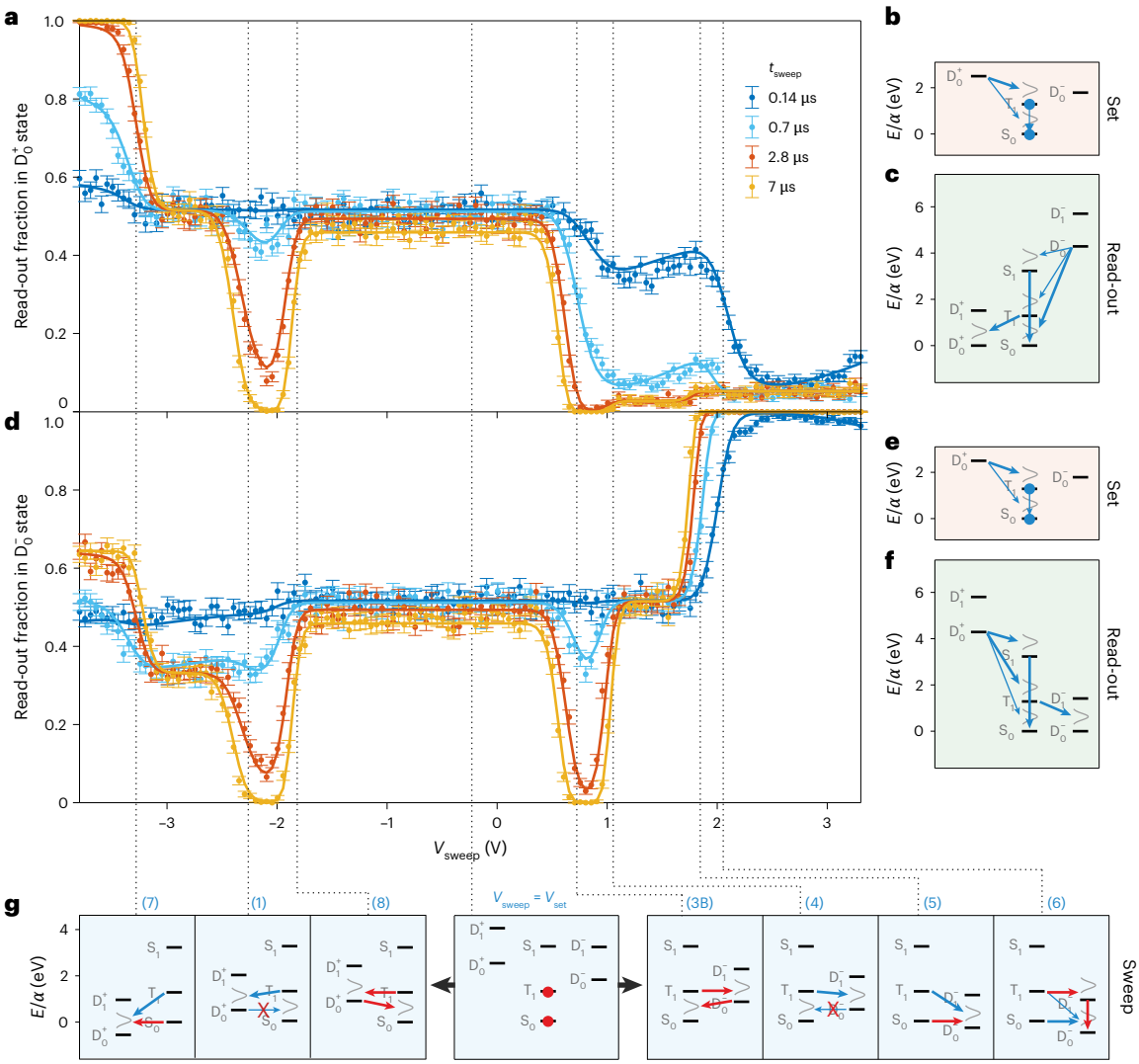

Fig. 4 | Excited-state spectroscopy of pentacene, initialized in the neutral charge state. a,**d**, Plot of the measured read-out fraction in the D_0^+ (**a**) and D_0^- (**d**) states, respectively, as a function of V_{sweep}. Measurements were performed with a voltage pulse sequence similar to Fig. 2a. A set pulse was used to initialize the molecule in S_0 or T_1, with approximately equal population (Methods). The read-out was at the S_0–D_0^+ ($V_{read\text{-}out} = -2.795$ V) or S_0–D_0^- ($V_{read\text{-}out} = 1.416$ V) degeneracies for **a** and **d**, respectively. Four different t_{sweep} were used, as indicated. Each data point corresponds to the normalized discrete counts of 640 pump–probe cycles and the error bars are ± s.d. (Methods). Solid lines represent fits to the data (Supplementary Sections 7 and 8). **b**,**c**,**e**,**f**, Many-body energy diagrams of the transitions taking place during the set pulse (**b**,**e**) and at the beginning of the read-out phase (**c**,**f**) for the spectra shown in **a** and **d**, respectively. **g**, Many-body energy diagrams of the assigned transitions happening around the sweep voltages indicated by the dotted lines. The transitions that correspond to those present in Fig. 3 are indicated with the same number. The arrows, crosses and dots are analogous to Fig. 3g. Note that if the sweep voltage is close to the set voltage (between (8) and (3B)), the population remains in the T_1 and S_0 states (see diagram at $V_{sweep} = V_{set}$). Only upon reducing or increasing V_{sweep} outside this range different transition channels open and/or close as indicated.

the molecule remains in D_0^+ owing to the Franck–Condon blockade[22,23] (Fig. 2b); hence at the end of each cycle, the state is read-out as D_0^+. Upon increasing V_{sweep} and thereby passing certain threshold voltages, labelled as (1, 2, ...), various transitions open or close. To facilitate the understanding, schematic diagrams in Fig. 3g show the possible transitions when passing the corresponding V_{sweep} threshold voltages. Upon V_{sweep} passing (1), a first tunnelling channel opens and an electron can tunnel from the tip into the HOMO resulting in S_0 (Fig. 3g). At (2) the electron can tunnel into the LUMO forming T_1. Importantly, this T_1 state has a lifetime of tens of microseconds[16] and is mapped onto D_0^+ during the read-out interval, while the population in S_0 remains in S_0 (ref. 16) (Fig. 3c).

In general, the assignment of features in the read-out signal to certain molecular transitions can be achieved by analysing the temporal evolution of the many-body state populations as follows. The transition rates associated to the tunnelling of electrons between tip and molecule can be controlled by the tip–sample distance and are chosen to be in the range of a fraction of a microsecond to a few microseconds (Methods). By contrast, the triplet-to-singlet transition occurs on a considerably longer timescale of tens of microseconds[16], whereas optically allowed transitions are typically much faster than the chosen charge-transition rates[24]. By varying the duration of the sweep pulse, the temporal evolution of the populations can be extracted, providing insight into the transition rates.

The assignment of other features in the spectra at increased sweep voltages follows the procedure as outlined above, namely by considering which transitions sequentially open and which time dependence is associated to it. If several transition pathways are available, their competition must be considered. The interpretation of the features was further guided by repeating the experiments with a different

https://doi.org/10.1038/s41565-024-01791-2

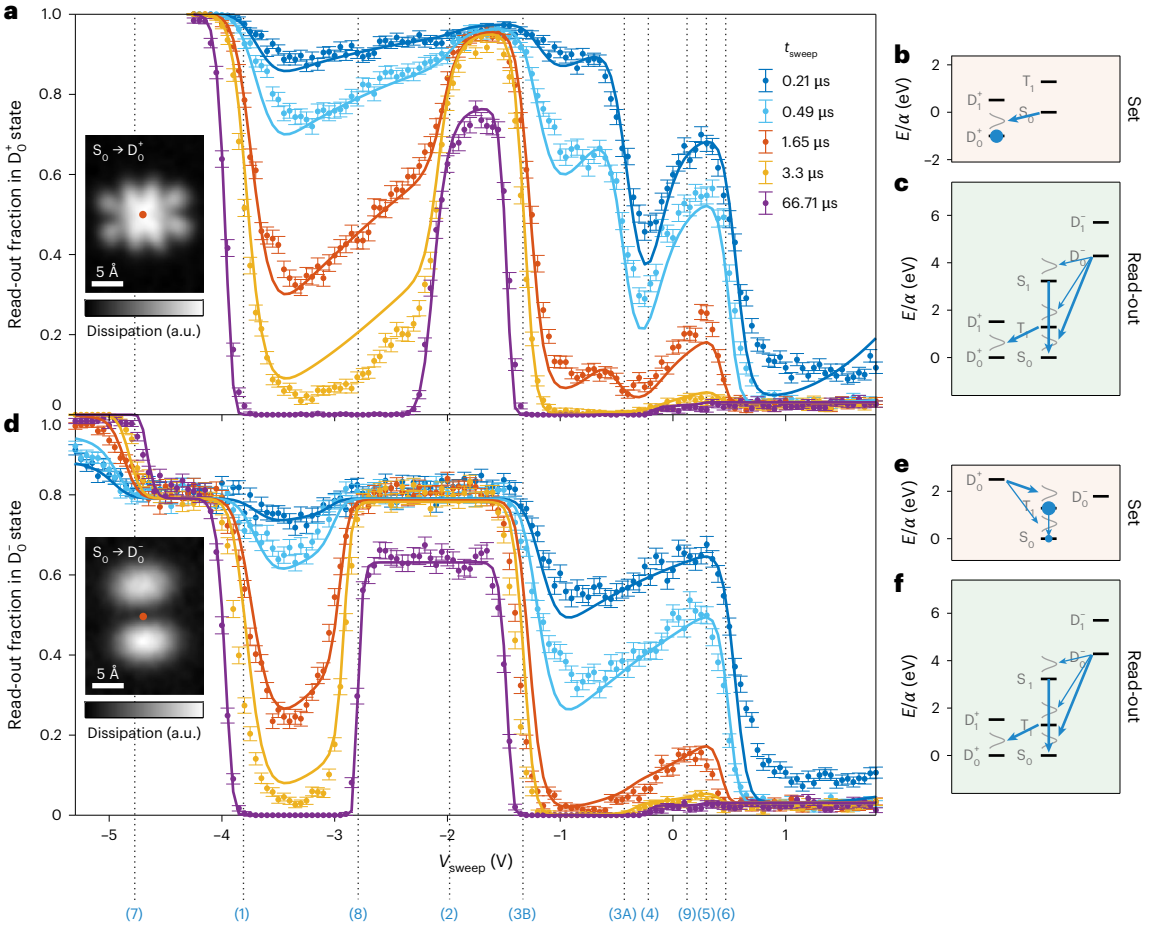

Fig. 5 | Excited-state spectroscopy of PTCDA. a,**d**, Plot of the measured read-out fraction in the D_0^+ state as a function of V_{sweep}. Measurements were performed with a voltage pulse sequence similar to Fig. 2a. A set pulse was used to initialize the molecule in the cationic state D_0^+ ($V_{set} = -5.30$ V) (**a**) and in the neutral charge state with 20% in S_0 and 80% in T_1 (**d**) (Methods). The read-out was at the S_0–D_0^+ degeneracy ($V_{read\text{-}out} = -4.30$ V). Five different t_{sweep} were used, as indicated. Each data point corresponds to the normalized discrete counts of 640 pump–probe cycles and the error bars are ± s.d. (Methods). Solid lines represent fits to the data (Supplementary Sections 7 and 8). The transition voltages are indicated by dotted lines with numbers indicating the assigned level alignment (see Figs. 2 and 3 and Supplementary Fig. 4 for the many-body energy diagrams). The insets show AC-STM images[15] measured for the same PTCDA molecule (oscillation amplitude $A = 1$ Å): $S_0 \rightarrow D_0^+$ (HOMO), $\Delta z = -2.3$ Å, $V_G = -4.55$ V, $V_{a.c.} = 1.2\ V_{pp}$; $S_0 \rightarrow D_0^-$ (LUMO), $\Delta z = -1.5$ Å, $V_G = 0.11$ V, $V_{a.c.} = 1.2\ V_{pp}$. Δz is relative to the set point $\Delta f = -1.75$ Hz at $V = 0$ V, $A = 3$ Å. The red dots indicate the position at which the spectra shown in Fig. 5 and Supplementary Fig. 10 were measured. Note that these images were taken at a tip–sample distance being 2.3 Å and 1.5 Å smaller than used for the excited-state spectroscopy, respectively. **b**,**c**,**e**,**f**, Many-body energy diagrams of the transitions taking place during the set pulse (**b**,**e**) and at the beginning of the read-out phase (**c**,**f**) for the spectra shown in **a** and **d**, respectively. These diagrams are not quantitative and for illustration purposes only.

read-out voltage, mapping the states onto D_0^- and S_0 instead of D_0^+ and S_0 (Fig. 3d). The assignment of the features in Fig. 3a,d is visualized in Fig. 3g and discussed in detail in Supplementary Sections 1, 3 and 6.

Importantly, next to the sequential opening of transitions starting at D_0^+, we can also detect transitions from the neutral state to the negatively charged state. For instance, we assign that at (3B) the $T_1 \rightarrow D_0^-$ pathway opens. From an additional experiment, we can discriminate transitions starting at D_0^+ from those starting at the neutral molecule. To this end, we initialized the molecule in the neutral state, approximately equally populating S_0 and T_1 (Methods). The results are shown in Fig. 4 and discussed in detail in Supplementary Sections 1, 4 and 6, while Extended Data Figs. 1 and 2 summarize all spectra and many-body diagrams for pentacene, respectively.

Many-body energies of pentacene

The relative energies of the electronic states can be derived by fitting the four sets of data shown in Figs. 3 and 4. To this end, we formulated a set of differential rate equations (Supplementary Section 7) based on the possible electronic transitions. On the basis of these rate equations, we fitted the four sets of data, including different t_{sweep}, simultaneously, obtaining one common set of fitting parameters for all data. The resulting fits are indicated by the solid lines in the plots of Figs. 3 and 4, resembling the data very well and thereby supporting our interpretation of the processes mentioned above. For details of the fitting procedure, see Supplementary Sections 7 and 8.

From these fits, a many-body energy diagram can be derived. To this end, the determined voltages have to be rescaled to energies taking into account the partial voltage drop across NaCl, that is, the lever arm[19–21] α. To derive α, we calibrated our energies using the S_0–S_1 energy difference determined as 2.26 eV by STM-induced luminescence for pentacene on NaCl(4 ML)/Ag(100)[25] (Supplementary Section 9). This calibration implies a voltage drop of 30 ± 2% across NaCl in our experiments, corresponding to a lever arm $\alpha = 0.70 \pm 0.02$. To account for potential influences of the environment (for example, presence of nearby step edges), as well as the possible influence of the metallic tip and its work function, the measurements were repeated for four different pentacene molecules, using four different metallic tip apexes. The many-body spectrum was derived from the averaged

https://doi.org/10.1038/s41565-024-01791-2

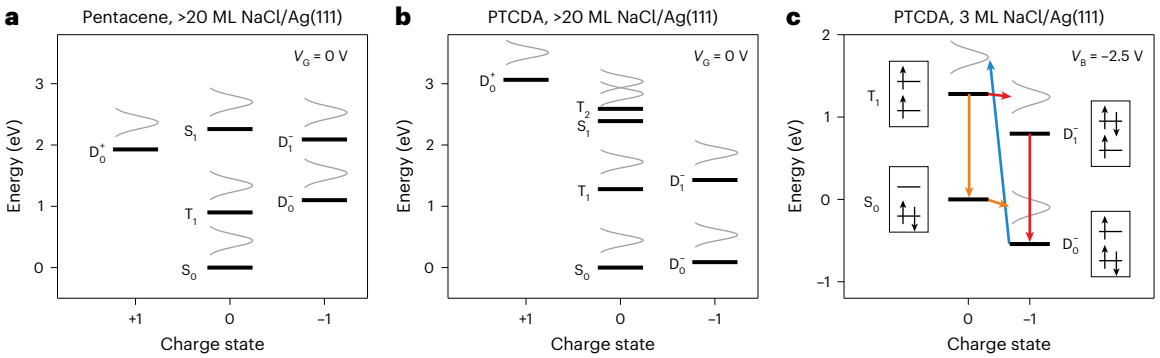

Fig. 6 | Many-body energy diagrams. a,**b**, Many-body energy diagrams of the electronic states of pentacene (**a**) and PTCDA (**b**) in the absence of gating, derived from fitting of excited-state spectroscopy measurements for four individual pentacene molecules and one PTCDA molecule, respectively. As in Fig. 2a, the rotated Gaussians (grey) indicate the broadening of the transitions owing to electron–phonon coupling, although they are not a property of the state, but of the transition being made. Here all relaxation energies and widths are set to their averaged values derived from fitting the experimental data. The relaxation energies are set to half of the reorganization energies. The excited triplet state T_2 of PTCDA is assumed to have one electron in the HOMO and the other in a state higher in energy than the LUMO, that is, a higher-lying unoccupied orbital (T_2 may also entail further contributions of other configurations). **c**, Many-body energy diagram of PTCDA extrapolated to ultrathin films (see Supplementary Section 11 for details) showing two possible pathways (orange and red) that could lead to the STM-induced luminescence signal with 1.33 eV photon energy for PTCDA[8,9] (both starting with the transition from the ground state D_0^- to T_1, blue arrow). This many-body energy diagram is drawn with respect to the chemical potential of the substrate and a bias voltage V_B of −2.5 V applied. That way, tunnelling events to or from the substrate result in transitions that lower the energy. By tip-molecule tunnelling charge transitions that increase the energy by maximally eV_B become possible, such as the $D_0^- \rightarrow T_1$ transition (involving molecule-tip tunnelling, blue arrow) shown here (note that at this voltage also the $D_0^- \rightarrow S_0$ transition is possible (not shown)). On ultrathin films the molecule will revert back to its ground state (here D_0^-) by molecule-substrate tunnelling. Next to the direct transition from T_1 to D_0^- (not shown), pathways via S_0 (orange) and D_1^- (red) are possible. Here the bias voltage also shifts (gates) the charged states with $-q(1-\alpha)V_B$, as explained in Supplementary Section 11, which is taken into consideration in the level alignment shown.

energies found for the four experiments (Supplementary Section 10 and Supplementary Table 2). To derive energy differences, we take the difference between two processes starting at the same state and ending in the two states of interest (for example, $D_0^+ \rightarrow S_0$ and $D_0^+ \rightarrow T_1$ for the S_0–T_1 energy difference). We find a S_0–T_1 energy difference of (0.90 ± 0.06) eV and a D_0^-–D_1^- energy difference of (0.99 ± 0.04) eV (Supplementary Section 10). The obtained S_0–T_1 energy difference of pentacene matches within uncertainty margins the value determined for pentacene in a tetracene crystal (0.86 ± 0.03) eV (ref. 26), despite the difference of environments.

Deriving energy differences as described above is subject to the implicit assumption that the relaxation energies[21] of the two involved transitions are similar. Because these transitions occur between the same charge states (for example, from positive to neutral), this assumption seems reasonable. Moreover, the validity of this assumption can be scrutinized experimentally by extracting the reorganization energies (sum of the relaxation energies) and the line widths from our spectroscopic data. To extract the reorganization energies, we consider pairs of transitions in opposing directions. For three of such pairs ($D_0^+ \leftrightarrow S_0$, $D_0^+ \leftrightarrow T_1$ and $S_0 \leftrightarrow D_0^-$), we find reorganization energies of roughly 0.9 eV, differing only slightly (see Supplementary Section 10 for details). The similar line widths of the many different charge transitions observed in our data suggest that also the corresponding relaxation energies are similar[23].

Excited-state spectroscopy on PTCDA

To demonstrate the wider applicability of this spectroscopic technique, we chose a system that is controversial in the literature. Specifically, the same STM-induced luminescence signal measured for PTCDA on thin NaCl films has been interpreted differently, on the one side, as phosphorescence of the neutral molecule[8] and, on the other side, as fluorescence of the anion[9], corresponding to either the $T_1 \rightarrow S_0$ (ref. 8) or the $D_1^- \rightarrow D_0^-$ (ref. 9) transition, respectively. Figure 5 shows the resulting spectra for PTCDA for read-out of the signal at the D_0^+–S_0 degeneracy. The analysis of the data was performed analogous to the one for pentacene, and the differences are discussed in Supplementary Section 5.

Fitting the data results in the curves shown in Fig. 5a,d. The calibration of the lever arm was done at the S_0–S_1 transition of a pentacene molecule that was co-adsorbed on the same NaCl terrace as the PTCDA molecule under study (Extended Data Fig. 3). From the fits, the energies of the S_0–S_1, S_0–T_1 and D_0^-–D_1^- differences were determined as (2.39 ± 0.11) eV, (1.28 ± 0.07) eV and (1.34 ± 0.08) eV, respectively.

These values match closely those reported in the STM-induced luminescence experiments[8,9] for PTCDA. The S_1–S_0 luminescence signal was reported to have an energy of 2.45 eV, while a second signal at 1.33 eV was controversially assigned either as T_1–S_0 or D_1^-–D_0^- (refs. 8,9). Our results indicate that both processes match in terms of energy the observed luminescence signal at 1.33 eV. The previous assignment of the luminescence signal as phosphorescence and, hence, to the T_1–S_0 transition was mainly based on comparing the photon energy with calculated energy differences of the two possible transitions[8]. Our data suggest that these two energies—extracted here experimentally—are too close to allow for an assignment of the transitions based on their energies.

Figure 6b shows the energy-level alignment that we determined for PTCDA on thick NaCl films (>20 ML). The alignment for ultrathin NaCl films (for example, 3 ML) can be extrapolated to comprehend how the molecule may cycle through different states during STM-luminescence experiments for a given bias voltage. For this extrapolation, one needs to consider increased screening[2,27–29], the possibility of a change in the work function[28,30], the different lever arm and tunnelling to the substrate. Guided by the energies that are available from the experiments on ultrathin films, the many-body diagram on ultrathin (3 ML) NaCl films can be derived (see Supplementary Section 11 for details).

In case of PTCDA on 3 ML NaCl films on Ag(111), the negative charge state is the ground state[8,31]. LUMO imaging at a threshold voltage of −0.55 V (ref. 8) suggests that at this voltage an electron tunnels out of the LUMO resulting in the S_0 state. From our results, we can infer that T_1 is 1.28 ± 0.07 eV higher in energy than S_0, which matches with the reported observation of a second peak in STS at a voltage of −2.05 V (ref. 8), if a lever arm α of 0.89 is taken into account (Supplementary Section 11). The threshold voltage of this $D_0^- \rightarrow T_1$ process corresponds

to the threshold voltage for observing the luminescence signal with a photon energy of 1.33 eV (ref. 8). This implies that the population of T_1 is important for the cycle leading to the luminescence signal. One interpretation of the observed luminescence is that it is due to phosphorescence from T_1 to S_0 (orange, Fig. 6c). However, T_1 being part of the luminescence cycle does not necessarily imply that the observed luminescence occurs from this state. Alternatively, T_1 can decay to D_1^- by an electron tunnelling from the substrate into the LUMO, opening the $D_1^- \rightarrow D_0^-$ luminescence transition (red, Fig. 6c). Note that both pathways become accessible at the voltage where T_1 can be formed. Which pathway is dominating is given by the rates of the involved processes: phosphorescence from T_1 to S_0 versus tunnelling from T_1 to D_1^-. Recently, the lifetimes of out-of-equilibrium charge states on 3 ML of NaCl were found to be on the timescale of 100 ps (ref. 11). By contrast, we find a T_1 state lifetime of approximately 300 µs on >20 ML NaCl (Extended Data Fig. 4) pointing towards a faster rate of T_1 decaying into D_1^- than into S_0. Note, however, that luminescence lifetimes can be strongly reduced on a few ML of NaCl. On the basis of our results, we can therefore not rule out the phosphorescence pathway. Note further that in case of a quinacridone molecule also both pathways were accessible, but in this case, luminescence mapping allows to disentangle the two pathways and assign the signal to luminescence of the charged exciton instead of phosphorescence[10].

Conclusion

The method that we introduce provides insights into individual electronic transitions of single molecules. It allows extracting the energy levels of ground and excited states for different charges, as well as the reorganization energies of redox transitions. In addition, relative rates of competing transitions can be accessed. We expect that the method can be applied to a wide range of molecules and even to multiple-charged ionic states, with the requirement of the presence of a long-lived state. Previous knowledge of some of the electronic properties is helpful but not necessary. Thereby, our method can be used for the quantification of excitation energies that are difficult to access otherwise, for example, those of triplet excitations[32]. Similarly, it can guide the understanding of STM-induced luminescence experiments on ultrathin insulating films, for which sequential and competing transitions are extremely challenging to characterize individually. Further, we anticipate that the spatial dependence of this spectroscopic method could be exploited for a spatial mapping of excited states. Furthermore, our pump–probe pulse scheme allows preparation of a molecule in a specific excited state and control of subsequent transitions. This level of control represents a toolset to guide, understand and engineer tip-induced chemical reactions as well as phosphorescence and fluorescence of individual molecules.

Online content

Any methods, additional references, Nature Portfolio reporting summaries, source data, extended data, supplementary information, acknowledgements, peer review information; details of author contributions and competing interests; and statements of data and code availability are available at https://doi.org/10.1038/s41565-024-01791-2.

References

1. Gross, L., Mohn, F., Moll, N., Liljeroth, P. & Meyer, G. The chemical structure of a molecule resolved by atomic force microscopy. *Science* **325**, 1110–1114 (2009).
2. Repp, J., Meyer, G., Stojković, S. M., Gourdon, A. & Joachim, C. Molecules on insulating films: scanning-tunneling microscopy imaging of individual molecular orbitals. *Phys. Rev. Lett.* **94**, 026803 (2005).
3. Baumann, S. et al. Electron paramagnetic resonance of individual atoms on a surface. *Science* **350**, 417–420 (2015).
4. Sellies, L. et al. Single-molecule electron spin resonance by means of atomic force microscopy. *Nature* **624**, 64–68 (2023).
5. Zhang, R. et al. Chemical mapping of a single molecule by plasmon-enhanced Raman scattering. *Nature* **498**, 82–86 (2013).
6. Qiu, X. H., Nazin, G. V. & Ho, W. Vibrationally resolved fluorescence excited with submolecular precision. *Science* **299**, 542–546 (2003).
7. Gutzler, R., Garg, M., Ast, C. R., Kuhnke, K. & Kern, K. Light–matter interaction at atomic scales. *Nat. Rev. Phys.* **3**, 441–453 (2021).
8. Kimura, K. et al. Selective triplet exciton formation in a single molecule. *Nature* **570**, 210–213 (2019).
9. Dolezal, J. et al. Real space visualization of entangled excitonic states in charged molecular assemblies. *ACS Nano* **16**, 1082–1088 (2022).
10. Jiang, S. et al. Many-body description of STM-induced fluorescence of charged molecules. *Phys. Rev. Lett.* **130**, 126202 (2023).
11. Kaiser, K., Lieske, L. A., Repp, J. & Gross, L. Charge-state lifetimes of single molecules on few monolayers of NaCl. *Nat. Commun.* **14**, 4988 (2023).
12. Klein, L. J. & Williams, C. C. Single-electron tunneling to insulator surfaces detected by electrostatic force. *Appl. Phys. Lett.* **81**, 4589–4591 (2002).
13. Bussmann, E., Kim, D. J. & Williams, C. C. Single-electron tunneling to insulator surfaces measured by frequency detection electrostatic force microscopy. *Appl. Phys. Lett.* **85**, 2538–2540 (2004).
14. Gross, L. et al. Measuring the charge state of an adatom with noncontact atomic force microscopy. *Science* **324**, 1428–1431 (2009).
15. Patera, L. L., Queck, F., Scheuerer, P. & Repp, J. Mapping orbital changes upon electron transfer with tunnelling microscopy on insulators. *Nature* **566**, 245–248 (2019).
16. Peng, J. et al. Atomically resolved single-molecule triplet quenching. *Science* **373**, 452–456 (2021).
17. Steurer, W., Fatayer, S., Gross, L. & Meyer, G. Probe-based measurement of lateral single-electron transfer between individual molecules. *Nat. Commun.* **6**, 8353 (2021).
18. Fatayer, S. et al. Probing molecular excited states by atomic force microscopy. *Phys. Rev. Lett.* **126**, 176801 (2021).
19. Wu, S. W., Nazin, G. V., Chen, X., Qiu, X. H. & Ho, W. Control of relative tunneling rates in single molecule bipolar electron transport. *Phys. Rev. Lett.* **93**, 236802 (2004).
20. Ihn, T. *Semiconductor Nanostructures: Quantum States and Electronic Transport* (Oxford Univ. Press, 2009).
21. Fatayer, S. et al. Reorganization energy upon charging a single molecule on an insulator measured by atomic force microscopy. *Nat. Nanotechnol.* **13**, 376–380 (2018).
22. Koch, J. & Von Oppen, F. Franck–Condon blockade and giant Fano factors in transport through single molecules. *Phys. Rev. Lett.* **94**, 206804 (2005).
23. Repp, J., Meyer, G., Paavilainen, S., Olsson, F. E. & Persson, M. Scanning tunneling spectroscopy of Cl vacancies in NaCl films: strong electron-phonon coupling in double-barrier tunneling junctions. *Phys. Rev. Lett.* **95**, 225503 (2005).
24. Lakowicz, J. R. *Principles of Fluorescence Spectroscopy* (Springer, 2006).
25. Kong, F. F. et al. Probing intramolecular vibronic coupling through vibronic-state imaging. *Nat. Commun.* **12**, 1280 (2021).
26. Burgos, J., Pope, M., Swenberg, C. E. & Alfano, R. R. Heterofission in pentacene-doped tetracene single crystals. *Phys. Status Solidi B* **83**, 249–256 (1977).
27. Zhang, L. et al. Electrically driven single-photon emission from an isolated single molecule. *Nat. Commun.* **8**, 580 (2017).
28. Imai-Imada, M. et al. Energy-level alignment of a single molecule on ultrathin insulating film. *Phys. Rev. B* **98**, 201403 (2018).

29. Scivetti, I. & Persson, M. Frontier molecular orbitals of a single molecule adsorbed on thin insulating films supported by a metal substrate: electron and hole attachment energies. *J. Condens. Matter Phys.* **29**, 355002 (2017).
30. Ploigt, H. C., Brun, C., Pivetta, M., Patthey, F. & Schneider, W. D. Local work function changes determined by field emission resonances: NaCl/Ag(100). *Phys. Rev. B* **76**, 195404 (2007).
31. Cochrane, K. A., Schiffrin, A., Roussy, T. S., Capsoni, M. & Burke, S. A. Pronounced polarization-induced energy level shifts at boundaries of organic semiconductor nanostructures. *Nat. Commun.* **6**, 8312 (2015).
32. Adhikari, S., Smit, R. & Orrit, M. Future paths in cryogenic single-molecule fluorescence spectroscopy. *J. Phys. Chem. C* **128**, 3–18 (2023).

Methods

Set-up and sample preparation

Experiments were carried out with a home-built atomic force microscope equipped with a qPlus sensor[33] (resonance frequency, $f_0 = 30.0$ kHz; spring constant, $k \approx 1.8$ kNm^{-1}; quality factor, $Q \approx 1.9 \times 10^4$) and a conductive Pt-Ir tip. The microscope was operated under ultrahigh vacuum (base pressure, $P < 10^{-10}$ mbar) at $T \approx 8$ K in frequency-modulation mode, in which the frequency shift Δf of the cantilever resonance is measured. The cantilever amplitude was 1 Å (2 Å peak-to-peak). AC-STM images[10] were taken in constant-height mode, at a reduced tip height as indicated by the negative Δz values (tip-height change with respect to the set point).

As a sample substrate, an Ag(111) single crystal was used that was prepared by sputtering and annealing cycles (annealing temperature, $T \approx 600$ °C). A thick NaCl film (>20 ML) was grown on half of the sample at a sample temperature of approximately 80 °C. In addition, a sub-ML coverage of NaCl was deposited on the entire surface at a sample temperature of approximately 35 °C. The tip was prepared by indentation into the remaining bare Ag(111) surface, presumably covering the tip apex with Ag. The measured molecules (pentacene and PTCDA) were deposited in situ onto the sample inside the scan head at a temperature of approximately 8 K.

The a.c. voltage pulses were generated by an arbitrary waveform generator (Pulse Streamer 8/2, Swabian Instruments), combined with the d.c. voltage, fed to the microscope head by a semi-rigid coaxial high-frequency cable (Coax Japan) and applied to the metal substrate as a gate voltage V_G. The high-frequency components of the pulses of V_G lead to spikes in the AFM signal because of the capacitive coupling between the sample and the sensor electrodes. To compensate these spikes, we applied the same pulses with opposite polarity and adjustable magnitude to an electrode that also capacitively couples to the sensor electrodes. Reflections and resonances in the gate-voltage circuitry were avoided by impedance matching, absorptive cabling and limiting the bandwidth of the external circuit to approximately 50 MHz. Experimental tests showed no indication of severe waveform distortions.

Spectroscopy pulse sequence and data acquisition

The spectra shown in Figs. 2–4 and Supplementary Figs. 2–4 and 7–10 were measured using a voltage pulse sequence similar to the one shown in Fig. 2a, as detailed in the captions of the figures.

To initialize in the D_0^+ state, the set-pulse voltage and duration were chosen such that it reliably brings the molecule in this state. We chose, therefore, a set pulse with a voltage that exceeds the relaxation energy for the $S_0 \rightarrow D_0^+$ transition having a duration that is much longer than the decay constant of this transition. Specifically, a set-pulse voltage was chosen that is 1 V lower than the D_0^+–S_0 degeneracy point, having a duration of 33.4 µs (one cantilever period). To initialize in the S_0 and T_1 states (for example, in Fig. 4), the set-pulse sequence consists of two parts: a pulse to bring the molecule to D_0^+ (the same parameters are used as for the pulse used to initialize in D_0^+) and another pulse to subsequently bring the molecule in the T_1 state. The second pulse is at −0.3 V (Fig. 4a,d, pentacene) (in general, it was set to $V_{\text{read-out}} + 2.5$ V for pentacene) or −1.8 V (Fig. 5d, PTCDA), respectively. Note that this pulse sequence has the same effect as the set and sweep pulse for the data at −0.3 V in Fig. 3a or −1.8 V in Fig. 5a, respectively. The duration of the second pulse determines the ratio of population of the T_1 and S_0 states, since the T_1 state will decay during this pulse to the S_0 state according to its molecule-specific lifetime. At the end of a 33.4 µs long second pulse of the set-pulse sequence with $V_{\text{set}} = -0.3$ V, the T_1 and S_0 population is 0.51 ± 0.01 and 0.49 ± 0.01, respectively, in case of pentacene in Fig. 4. By contrast, the same set-pulse length with $V_{\text{set}} = -1.8$ V gives a T_1 and S_0 population of 0.79 ± 0.01 and 0.21 ± 0.01, respectively, for PTCDA in Fig. 5d. Supplementary Fig. 3 shows data for pentacene with different initial populations of the T_1 and S_0 states. To this end, pulse durations of 33.4 µs and 100.1 µs were chosen.

A cantilever oscillation amplitude of 1 Å (2 Å peak-to-peak) was chosen to optimize the signal-to-noise ratio for charge-state detection[34]. The oscillation amplitude modulates the tip height and thereby induces variations in the tunnelling rate and slight variations in the lever arm of the gate voltage. To minimize these effects, the voltage pulses were synchronized with the cantilever oscillation period, such that they started 2 µs before the turn-around point at minimal tip–sample distance. Furthermore, the sweep pulses were chosen to be short, such that the entire sweep pulse occurs around the point of minimal tip–sample distance. If this was not possible, full cantilever-period pulses were chosen. The resulting minor influence of the cantilever's oscillation amplitude on the excited-state spectroscopy data was neglected in the modelling and, hence, in the fitting. For example, neglecting the cantilever's oscillation likely causes the deviation between the fit and the data shown in Fig. 5a between voltages (1) and (2) for $t_{\text{sweep}} = 3.3$ µs (yellow curve).

The tip height was chosen by setting the decay of D_0^+ into S_0 at a voltage of 1 V above the voltage corresponding to the degeneracy of the D_0^+ and S_0 states to around 1.5 µs. This tip height is sufficiently large to minimize tunnelling events between the two bistable states during the read-out phase of the pulse sequence, which gives a lower limit to the tip–sample height. The upper limit of the tip–sample height is given by the requirement that the tunnelling rates should be much faster than the slowest triplet decay rate. Typically, these two requirements restrict the possible tip–sample heights to a small range (less than 2 Å) around the relatively large tip–sample height used (estimated to be 9 Å; Supplementary Section 7).

The shortest sweep pulse duration was then chosen such that at the largest V_{sweep} used, the read-out fraction in the D_0^+ state was around 0.10. This allowed the observation of transitions at positive voltages, such as (6) in Fig. 3a. By contrast, a longer sweep pulse duration is crucial for the observation of transitions (7), (1) and (8). The longest pulse duration was, therefore, typically set such that the fraction in the D_0^+ state was close to zero at a voltage of 1 V above the voltage corresponding to the degeneracy of the D_0^+ and S_0 states. Two or three additional sweep pulse durations were chosen in between the determined shortest and longest pulse duration to improve the reliability of the fitting.

To determine the population in the two charge states during the read-out, the voltage pulse sequences were typically repeated 8 times per second for 80 s for every sweep voltage. The error bars were derived as the s.d. of the binominal distribution (see below). The measurements were performed in constant-height mode. To correct for vertical drift, for example, owing to piezo creep, the tip–sample distance was typically reset every 15 min by shortly turning on the Δf-feedback. Lateral drift was corrected every hour by taking an AC-STM image (similarly as described in ref. 15) and cross-correlating it with an AC-STM image taken at the beginning of the measurement.

Data analysis

For data analysis, trigger pulses synchronized with the pump–probe voltage pulses were used to identify the start of every read-out interval (dotted lines in Fig. 2c). The remaining effect of the capacitive coupling described above as well as a possible excitation of the cantilever owing to the few µs sweep voltage pulses can cause spikes at the beginning of every read-out period (not present for the data in Fig. 2c), which were removed from the data trace. Subsequently, every read-out interval was low-passed and it was determined if the averaged frequency shift during this interval was above or below the value centred between the frequency shifts of the two charge states. Counting the number of read-out intervals for which the frequency shift was above this value and dividing it by the total number of intervals gives the read-out fraction in the charge state. For the metal tips that we have used, the D_0^+ and D_0^- states always had a less negative frequency shift compared with S_0 (at the respective read-out voltage).

Error bars

The uncertainty on the determined read-out fraction in the charge state is dominated by the statistical uncertainty. Because of the two possible outcomes (charged or neutral), the statistics of a binomial distribution apply (ref. 16). The s.d. on the counts in a charged state N_c is, therefore, given by

$$\sigma_{Nc} = \sqrt{\frac{N_0 N_c}{N_c + N_0}},$$

with N_0 being the counts in the neutral state. The error bars on the measured fractions in the charged state are then given by

$$\Delta_c = \frac{\sigma_{Nc} + 1}{N_c + N_0},$$

where the second term in the numerator accounts for the discrete nature of N_c.

Data availability

The data supporting the findings of this study are available in the University of Regensburg Publication Server with the identifier 'https://doi.org/10.5283/epub.58766' (ref. 35). Source data are provided with this paper.

References

33. Giessibl, F. J. High-speed force sensor for force microscopy and profilometry utilizing a quartz tuning fork. *Appl. Phys. Lett.* **73**, 3956–3958 (1998).
34. Giessibl, F. J. Advances in atomic force microscopy. *Rev. Mod. Phys.* **75**, 949 (2003).
35. Sellies, L., Eckrich, J., Gross, L., Donarini, A. & Repp, J. Data archive of 'Single-electron shuttling enables time-resolved excited-state spectroscopy of individual molecules'. *University of Regensburg Publication Server* https://doi.org/10.5283/epub.58766 (2024).

Acknowledgements

We thank S. Bleher, R. Spachtholz, S. Fatayer, T.-C. Hung and A. Rosławska for discussions and C. Rohrer for technical support. Funding from the ERC Synergy Grant MolDAM (no. 951519) and the Deutsche Forschungsgemeinschaft (DFG, German Research Foundation) through RE2669/6-2 and 314695032—SFB 1277 is gratefully acknowledged.

Author contributions

L.S. and J.R. conceived the experiments and L.S. and J.E. carried them out. L.S., L.G. and J.R. analysed the experimental results. L.S., A.D. and J.R. devised the model and L.S. and J.R. simulated the data. L.S. and J.R. wrote the paper. All authors discussed the results and their interpretation and revised the paper.

Competing interests

The authors declare no competing interests.

Additional information

Extended data is available for this paper at https://doi.org/10.1038/s41565-024-01791-2.

Supplementary information The online version contains supplementary material available at https://doi.org/10.1038/s41565-024-01791-2.

Correspondence and requests for materials should be addressed to Lisanne Sellies or Jascha Repp.

Peer review information *Nature Nanotechnology* thanks Yannick Dappe, Zhen-Chao Dong, Harry Mönig and Martin Švec for their contribution to the peer review of this work.

https://doi.org/10.1038/s41565-024-01791-2

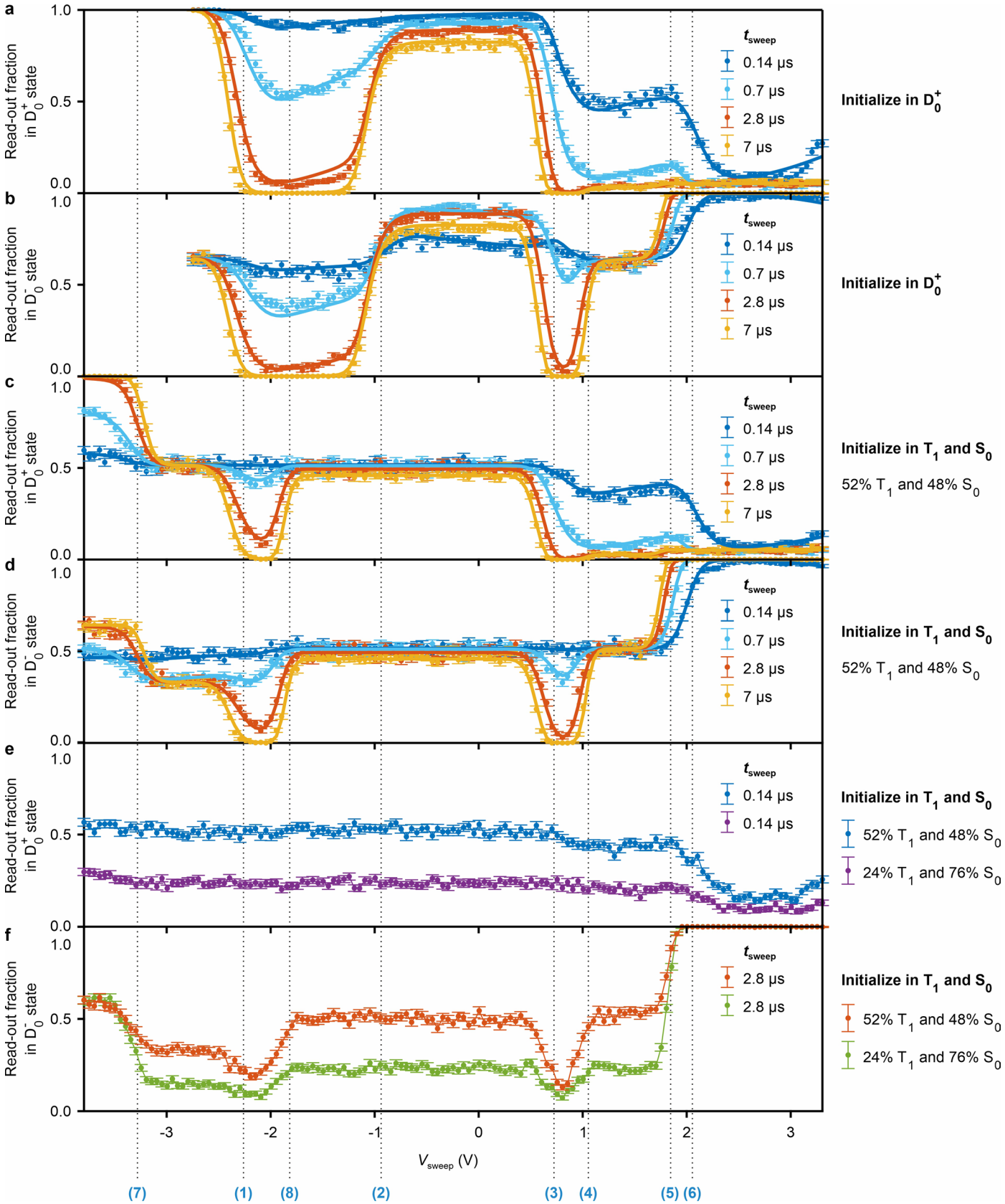

Extended Data Fig. 1 | Excited-state spectroscopy on pentacene, for different initial and read-out states. The same spectra are shown as in Fig. 3 (**a**, **b**), Fig. 4 (**c**, **d**) and Fig. S3 (**e**, **f**). The populations of the states at the beginning of the sweep pulse are indicated. The read-out was at the S_0-D_0^+ degeneracy for **a**, **c** and **e** and at the S_0-D_0^- degeneracy for **b**, **d** and **f**. The features are indicated by dotted lines with numbers indicating the assigned level alignment (the many-body diagrams are shown in Extended Data Fig. 2). Each data point corresponds to the normalized discrete counts of 640 pump–probe cycles and the error bars are ± s.d.; see Methods.

https://doi.org/10.1038/s41565-024-01791-2

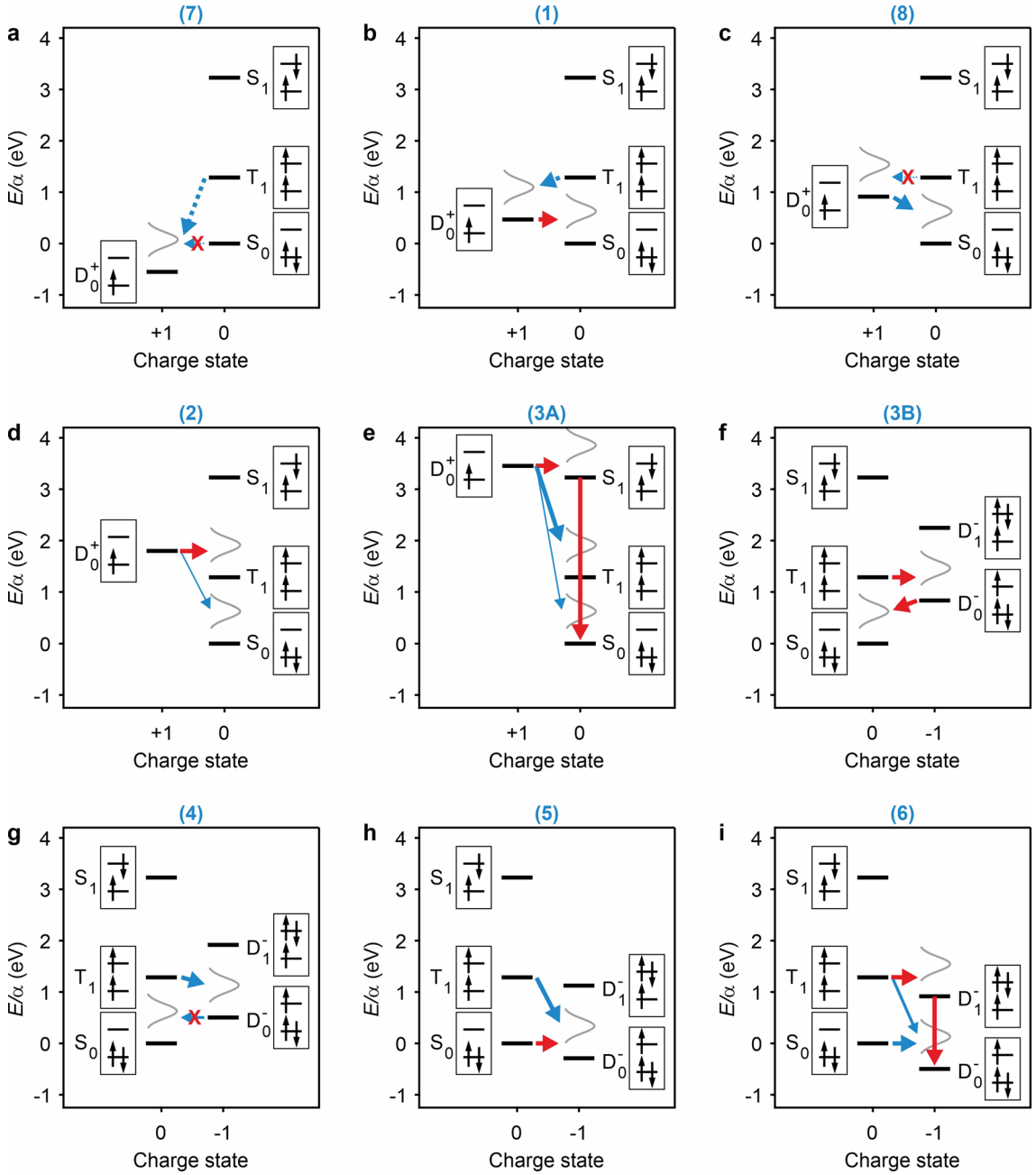

Extended Data Fig. 2 | Many-body energy diagrams of the assigned transitions for pentacene. a-i, Many-body diagrams corresponding quantitatively to the transition voltages indicated by numbers in Ext. Data Fig. 1 (as well as Figs. 3, 4, S2 and S3) as well as qualitatively to the transition voltages for the data of PTCDA shown in Fig. 5. For clarity only a subset of all levels is shown in each panel. The process(es) that cause the change in the read-out fraction for every numbered threshold voltage are represented by red arrows (opening of a transition) and crosses (closing of a transition). The dotted lines in **a**, **b** and **c** indicate transitions only present for initialization in the T_1 and S_0 state (not occurring during the sweep pulse when initializing in D_0^+). The relative thicknesses of the different arrows connecting two charge states (for a given subfigure) roughly indicates the ratio of the rates governed by the different tunneling barriers (Supplementary Section 2).

https://doi.org/10.1038/s41565-024-01791-2

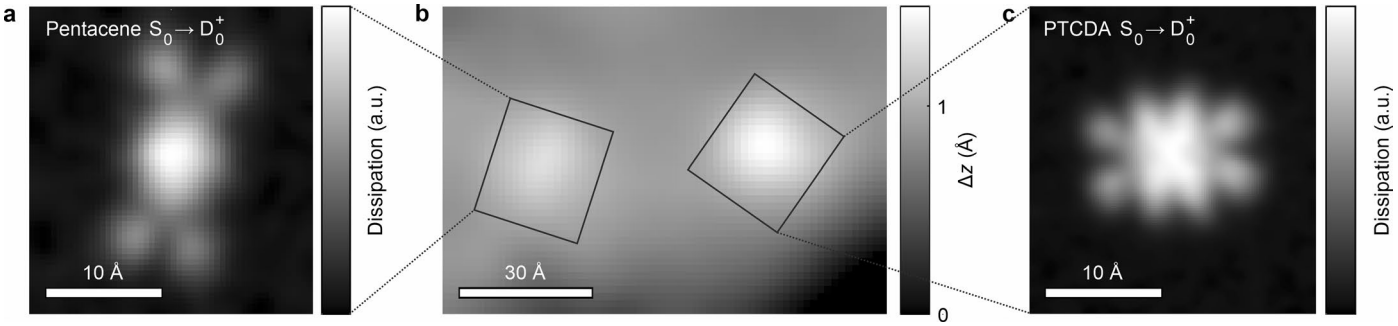

Extended Data Fig. 3 | AFM images. b, AFM topography image of the NaCl-covered surface with the pentacene and PTCDA molecules for which excited-state spectroscopy data was measured (setpoint $\Delta f = -1.65$ Hz at $V = 0$ V, $A = 3$ Å). In the lower-right corner of the image a descending NaCl step edge is seen. The corresponding excited-state spectroscopy data is shown for the PTCDA molecule, the spectroscopy of which is presented in Fig. 5. The resulting fitting parameters for pentacene and PTCDA are listed in Table S1 (as pentacene 2 and as PTCDA). **a**, **c**, AC-STM images[15] of the $S_0 \rightarrow D_0^+$ transition (HOMO) of the two molecules in **b** (oscillation amplitude $A = 1$ Å, pentacene (**a**): $\Delta z = -3.0$ Å, $V_G = -2.90$ V, $V_{a.c.} = 1.2\ V_{pp}$, and PTCDA (**c**): $\Delta z = -2.3$ Å, $V_G = -4.55$ V, $V_{a.c.} = 1.2\ V_{pp}$). Δz is given with respect to the setpoint $\Delta f = -1.75$ Hz at $V = 0$ V, $A = 3$ Å.

https://doi.org/10.1038/s41565-024-01791-2

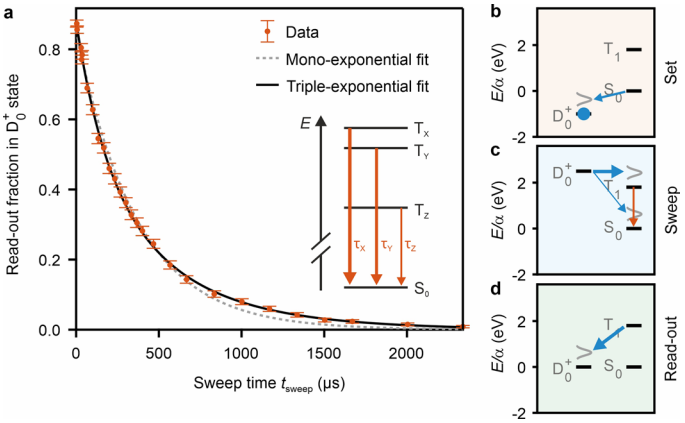

Extended Data Fig. 4 | Triplet decay of PTCDA. a, Plot of the measured read-out fraction in the D_0^+ state versus t_{sweep} for a PTCDA molecule on >20 monolayers NaCl/Au(111). Measurements were performed with a voltage pulse sequence similar to Fig. 2a, which was introduced in ref. 16. At the end of the set pulse (V_{set} = −4.54 V), the D_0^+ state is populated. A sweep voltage of −1.04 V was chosen to populate the T_1 and S_0 states. The read-out was at the S_0-D_0^+ degeneracy ($V_{read\text{-}out}$ = −3.54 V), mapping the T_1 state population onto the D_0^+ state. The voltage pulse sequence was repeated 8 times per second for 160 seconds for every t_{sweep}, and the error bars were derived for the normalized discrete counts of these 1280 pump–probe cycles as ± s.d. of the binominal distribution (Methods). The resulting decay with increasing t_{sweep} reflects the decay of the T_1 state population, which can be well fitted with a triple-exponential decay (black). Averaging over three measurements (on two individual molecules) yields decay constants of 350 ± 43 μs, 170 ± 13 μs and 671 ± 62 μs. These three lifetimes are associated with the zero-field-split substates of T_1. This is confirmed by the zero-field triplet state ESR spectra which were measured for individual PTCDA molecules on the same substrate via AFM, as reported in ref. 4. **b**, Many-body energy diagrams of the transitions taking place during the set and sweep pulse and at the beginning of the read-out phase for the T_1-state lifetime measurement shown in **a**. The arrows and dots are analogous to Fig. 3g.